AGU PUBLICATIONS

JGR

Journal of Geophysical Research: Earth Surface

RESEARCH ARTICLE
10.1002/2014JF003346

Key Points:
- Connection between flow patterns, bed load pathways, and morphological change
- Oscillatory dynamics of scour and fill during high-flow events in a braided river
- Coupled TLS and aDcp surveys in a fluvial system reveal process and form dynamics

Supporting Information:
- Readme
- Figure S1
- Figure S2

Correspondence to:
R. D. Williams,
rdw5@aber.ac.uk

Citation:
Williams, R. D., C. D. Rennie, J. Brasington, D. M. Hicks, and D. Vericat (2015), Linking the spatial distribution of bed load transport to morphological change during high-flow events in a shallow braided river, *J. Geophys. Res. Earth Surf.*, *120*, doi:10.1002/2014JF003346.

Received 29 SEP 2014
Accepted 19 FEB 2015
Accepted article online 23 FEB 2015

Linking the spatial distribution of bed load transport to morphological change during high-flow events in a shallow braided river

R. D. Williams[1], C. D. Rennie[2], J. Brasington[3], D. M. Hicks[4], and D. Vericat[1,5,6]

[1]Department of Geography and Earth Sciences, Aberystwyth University, Aberystwyth, UK, [2]Department of Civil Engineering, University of Ottawa, Ottawa, Ontario, Canada, [3]School of Geography, Queen Mary University of London, London, UK, [4]National Institute of Water and Atmospheric Research, Christchurch, New Zealand, [5]Fluvial Dynamics Research Group (RIUS), Department of Environment and Soil Sciences, University of Lleida, Lleida, Spain, [6]Hydrology Section, Forest Sciences Center of Catalonia, Solsona, Spain

Abstract This paper provides novel observations linking the connections between spatially distributed bed load transport pathways, hydraulic patterns, and morphological change in a shallow, gravel bed braided river. These observations shed light on the mechanics of braiding processes and illustrate the potential to quantify coupled material fluxes using remotely sensed methods. The paper focuses upon a 300 m long segment of the Rees River, New Zealand, and utilizes spatially dense observations from a mobile acoustic Doppler current profiler (aDcp) to map depth, velocity, and channel topography through a sequence of high-flow events. Apparent bed load velocity is estimated from the bias in aDcp bottom tracking and mapped to indicate bed load transport pathways. Terrestrial laser scanning (TLS) of exposed bar surfaces is fused with the aDcp surveys to generate spatially continuous digital elevation models, which quantify morphological change through the sequence of events. Results map spatially distributed bed load pathways that were likely to link zones of erosion and deposition. The coherence between the channel thalweg, zone of maximum hydraulic forcing, and maximum apparent bed load pathways varied. This suggests that, in places, local sediment supply sources exerted a strong control on the distribution of bed load, distinct from hydraulic forcing. The principal braiding mechanisms observed were channel choking, leading to subsequent bifurcation. Results show the connection between sediment sources, pathways, and sinks and their influence on channel morphology and flow path directions. The methodology of coupling spatially dense aDcp surveys with TLS has considerable potential to understand connections between processes and morphological change in dynamic fluvial settings.

1. Introduction

Braided rivers are fundamentally unstable due to high rates of lateral bank migration associated with rapid erosion and deposition [*Lane et al.*, 1995; *Ashmore*, 2013]. Linking the associated patterns of hydraulics and bed load transport that contribute to such rapid channel change is essential to gain insight into the physical mechanisms of braiding over a wide range of spatial scales. This approach demands concurrent, spatially distributed measurements, which represents a nontrivial task in the natural environment. These challenges are especially apparent during periods of high flow, when considerable morphological activity occurs, but obtaining measurements is challenging, particularly in shallow gravel bed braided rivers where crewed boats cannot be used safely and the bed is obscured by turbid water. Nevertheless, acquiring data through a range of flows is necessary to examine the coherence between zones of erosion and deposition.

1.1. Bed Load Transport and Morphodynamics

Two interrelated issues demand attention to further understand the links between bed load transport, flow dynamics, and morphological change. These are (i) determining the form and scale of connections between zones of erosion and deposition and (ii) the difficulty of obtaining distributed measurements of flow and bed load transport in shallow, gravel bed braided rivers due to their wide, shallow, fast, and turbulent flows. These issues are expanded upon below; section 1.2 then assesses how contemporary remote survey technologies can be used to address these problems in shallow, gravel bed braided rivers.

The first issue is the need for distributed measurements of flow and sediment transport to support the interpretation of morphological change. Pioneering studies that identified erosional and depositional

mechanisms of braided river channel change primarily relied upon the planimetric analysis of aerial or oblique photography [*Ashmore*, 1991; *Ferguson*, 1993]. The availability of high-resolution digital elevation models (DEMs) of braided river topography and the application of DEM differencing [*Brasington et al.*, 2000; *Williams*, 2012] with suitable uncertainty analysis [*Wheaton et al.*, 2010] have enabled the mapping of spatial patterns of braided river erosion and deposition [e.g., *Hicks et al.*, 2002; *Brasington et al.*, 2003; *Lane et al.*, 2003; *Milan et al.*, 2007; *Williams et al.*, 2011; *Wheaton et al.*, 2013; *Lallias-Tacon et al.*, 2014]. The classification of "morphodynamic signatures" from DEMs of Differences (DoDs) has considerable potential for identifying mechanisms of channel change [*Wheaton et al.*, 2013]. However, while DoDs offer insight into the pattern of channel changes between surveys, connection between zones of erosion and deposition can only be inferred indirectly. To close this circle, in addition to capturing snapshots of topography, observations of bed load transport along key flow pathways are needed [*Ashmore and Gardner*, 2008; *Ashmore*, 2013]. Moreover, the frequency of repeat topographic and bed load transport pathway surveys needs to be sufficiently high to account for bed level compensation effects associated with cycles of erosion and deposition. Establishing the connection between the supply, transport, and deposition of sediment is also needed to improve the parameterization and testing of physics-based [*Nicholas*, 2013a] numerical morphodynamic models of braided rivers [e.g., *Jang and Shimizu*, 2005; *Nicholas*, 2013b, 2013c; *Schuurman et al.*, 2013; *Ziliani et al.*, 2013].

The second, interconnected issue is to relate the spatial distribution of hydraulics and bed load transport during high flows. The shallow vertical relief of braidplain topography results in rapid expansion of inundated area with increasing discharge, facilitated by the reoccupation of high stage channels. However, with increased discharge accommodated largely by changes in wetted width, the frequency distributions of water depth, depth-averaged velocity, and shear stress may remain largely unchanged except in very high flows [*Mosley*, 1982, 1983; *Ashmore and Sauks*, 2006]. Such flood conditions pose severe logistical challenges for acquiring spatially distributed measurements of bed load transport and hydraulics in shallow, gravel bed rivers. Bankside measurements are of limited value, while in-channel conditions are too dangerous for wading and flows are too shallow to navigate by boat. Existing evidence from physical sampling suggests that bed load transport in braided rivers may be confined to narrow threads [*Thompson*, 1985; *Gomez*, 1991; *Ferguson et al.*, 1992; *Warburton*, 1992]. However, such evidence is often interpreted with scepticism due to an awareness of the temporal variation in bed load transport and the difficulty in acquiring spatially distributed measurements at high flow. Moreover, in the absence of spatially distributed flow depth and velocity measurements, the relation between the location of narrow bed load transport bands, the thalweg, and zones of greatest hydraulic forcing are not known. There is thus a need to develop and test field methodologies that can be deployed in shallow, gravel bed braided rivers to map both flow dynamics and bed load transport pathways simultaneously during high flows.

1.2. Opportunities From Contemporary Remote Sensing Technologies

In response to these issues, it is useful to consider how existing sampling and remote sensing techniques can be used to shed light on the linkages between bed load transport pathways, flow dynamics, and morphological change. The first step in connecting zones of erosion and deposition is to produce DoDs that are characterized by high signal-to-noise ratios. *Williams et al.* [2014] identified a threefold set of challenges associated with surveying braided river topography which they deemed the "morphological," "wetted channel," and "mobility" problems. To address these challenges, they presented a data fusion methodology that combined mobile terrestrial laser scanning (TLS) with optical bathymetric mapping to produce a DEM that had vertical errors of 0.03 and 0.12 m in exposed and inundated areas, respectively. The second step in identifying connections between zones of erosion and deposition requires bed load transport measurements, a notoriously challenging task that does not always achieve acceptable levels of accuracy [*Wilcock et al.*, 2001]. Traditional techniques, including pressure difference bed load samplers [*Helley and Smith*, 1971] or portable bed load traps [*Hicks and Gomez*, 2005], are of limited value for acquiring spatially distributed measurement not only due to bias in their sampling efficiency [*Glysson*, 1993; *Childers*, 1999; *Bunte et al.*, 2003; *Vericat et al.*, 2006] but because sampling also requires prolonged steady flow. Bed load traps or settling ponds yield more stable estimates compared to at-a-point bed load samplers [*Reid et al.*, 1980; *Garcia et al.*, 1999; *Habersack et al.*, 2001; *Vericat and Batalla*, 2010; *Rickenmann et al.*, 2012] but cannot capture spatial variability and are unsuitable for deployment in wide rivers. Indirect or surrogate observational methods [*Barton et al.*, 2010; *Gray et al.*, 2010; *Burtin et al.*, 2011] offer new opportunities to help quantify bed

load transport, although these approaches require calibration against reference rates which are themselves inevitably bedevilled by uncertainty. Active acoustic methods have been used to measure apparent bed load velocity, v_a, by determining the bias in aDcp bottom-track estimates of sensor velocity using independent GPS observations [*Rennie et al.*, 2002]. Coincident direct sampling of bed load and active acoustic surveys at quasi-stationary points shows that apparent bed load velocity is correlated with bed load transport rate [*Rennie and Villard*, 2004; *Gaeuman and Pittman*, 2007; *Holmes*, 2007; *Villard et al.*, 2005; C. D. Rennie et al., Calibration of aDcp apparent bed load velocity to bed load transport rate, in Gravel Bed Rivers: Processes and Disasters, edited by D. Tsutumi and J. Laronne, John Wiley, Chichester, West Sussex, U. K., in review]. A major advantage of v_a compared to physical bed load sampling is that it can be measured from a moving boat and thus used to map spatial variability in bed load throughout a reach [*Rennie and Millar*, 2004; *Jacobson et al.*, 2009; *Rennie and Church*, 2010; *Jamieson et al.*, 2011b, 2011a]. Mapping v_a during morphologically competent flows thus provides an opportunity to study bed load transport pathways and connect zones of erosion and deposition.

Acquiring aDcp measurements during high flows is straightforward, if flows are sufficiently deep for navigation using crewed boats, and has provided insight into flow structures of large sand bed rivers [*Muste et al.*, 2004; *Dinehart and Burau*, 2005; *Parsons et al.*, 2005, 2007; *Szupiany et al.*, 2009, 2012; *Parsons et al.*, 2013]. Where transects are tightly spaced in a streamwise direction, depth-averaged [*Rennie and Millar*, 2004; *Rennie and Church*, 2010; *Guerrero and Lamberti*, 2011] or three-dimensional [*Jamieson et al.*, 2011a; *Tsubaki et al.*, 2012] hydraulic data have been interpolated to produce spatially continuous maps of depth and velocity. Spatially distributed apparent bed load velocity has also been mapped in large, gravel bed rivers [*Rennie and Church*, 2010]. While crewed operations offer opportunities to study hydrodynamic processes in large rivers, shallow braided rivers with complex anabranch networks pose hazards for navigation with the necessary large boats. Access may sometimes be afforded using jet boats; however, the high speed of these vessels makes them unsuitable for aDcp sampling. At present, the most feasible sampling option is therefore to utilize tethered boats to acquire transect data [*Entwistle et al.*, 2010; *Riley and Rhoads*, 2012]. This approach requires operators to stand on either side of an anabranch, and this is often feasible in all but the highest of flows. Moreover, assessing the utility of v_a and flow pattern mapping using a tethered approach will provide the foundations for the development of suitable control systems that will enable remote-controlled boats, with aDcp platforms (e.g., OceanScience Q-Boat, HR Wallingford ARC-Boat), to acquire closely spaced transect surveys in relatively high-velocity flow.

1.3. Aim and Structure

This paper aims to mesh precise and accurate geomatics and acoustic technologies to investigate connections between morphological evolution, bed load transport pathways, and flow patterns during high-flow events using a comprehensive set of field surveys from the braided Rees River, New Zealand. The simultaneous acquisition of TLS and aDcp surveys and associated data processing addresses the two issues identified above, namely, connecting zones of erosion and deposition and mapping bed load pathways and flow pattern during high flows. The resulting synoptic surveys cover a wide range of competent discharges, and as far as we are aware, similar data have not previously been presented for a shallow, gravel bed river. This paper builds upon a preliminary field survey described by *Rennie* [2012].

The paper is structured in four sections. In the first section, we describe the characteristics of the Rees River and the study reach. The subsequent section describes the aDcp and TLS surveys; the procedures used to map depth, velocity, v_a, and topography; and the technique used to calculate DoDs. Next, the results from five sets of surveys are presented and interpreted. Finally, a discussion considers how the deployment of TLS and aDcp addresses the challenge of inferring links between the spatial distribution of bed load, morphological change, and braiding mechanisms.

2. Study Area

The Rees River drains a 420 km^2 catchment in the Southern Alps of New Zealand. *Cook et al.* [2013] describe the geomorphology of the Rees River. *Williams et al.* [2013] describe catchment hydrology and broad-scale morphodynamics of the study reach. The specific study reach is located toward the downstream end, in a 2.5 km long braided section (with a longitudinal slope of 0.005) that had previously been monitored through a sequence of high-flow events from September 2009 to May 2010 [*Brasington*, 2010; *Williams et al.*, 2011, 2014]. Figure 1a shows an aerial image of the study area that was acquired on 27 February 2011, during the

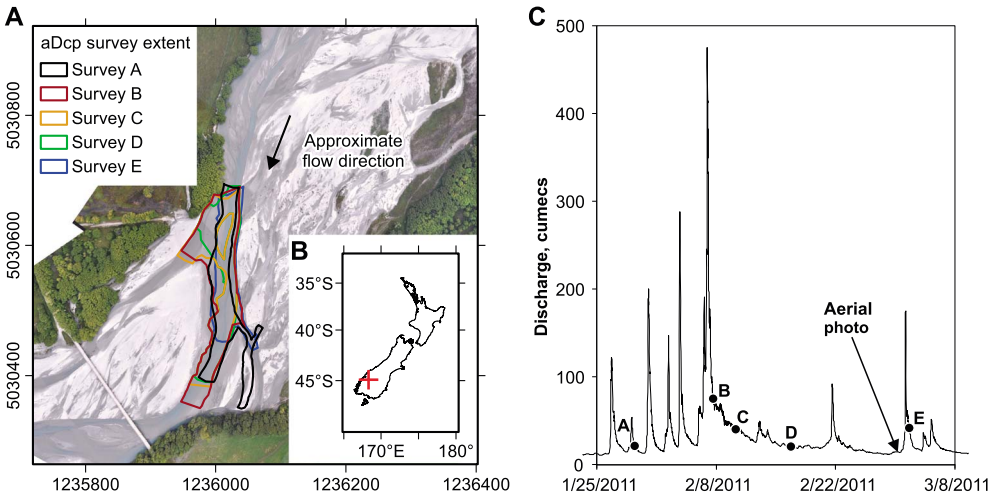

Figure 1. (a) Extent of aDcp surveys and aerial image of the study area. The aerial image was acquired on 27 February 2011 before the penultimate high-flow event and survey E (see hydrograph shown in Figure 2). The image is a mosaic of three nonmetric aerial photos that were acquired from a R-22 helicopter using a 12 megapixel single lens reflex Nikon D_{90} camera, with fixed 28 mm lens and a polarizing filter to minimize Sun glint. Each image was georeferenced using natural object control points that were surveyed using RTK-GPS. Maps showing the topography of the Rees River catchment, and its location in New Zealand, can be found in *Williams et al.* [2013, 2014]. The coordinate grid is in New Zealand Transverse Mercator. (b) Location of the study area in New Zealand. In the WGS84 coordinate system, the upstream boundary of the study reach is at 44°47′05″S, 168°23′57″E. (c) Rees River hydrograph showing survey times and timing of aerial image. The gauging station was located approximately 8 km upstream of the study site, in a bedrock gorge. Since flow was routed across the braidplain during high-flow events, the total flow recorded at Invincible was not necessarily equal to the flow entering the braid-bar unit. However, the hydrograph indicates the flow conditions during each survey.

monitoring campaign undertaken for this paper. The extent of each survey is indicated in the figure. Upstream, the main anabranch flowed close to the braidplain's true right bank. Approximately 200 m upstream, this principal anabranch bifurcated around a midchannel bar, which extended for about 120 m downstream. This bar was dissected by chutes indicative of a large pulse of sediment moving downstream. The main anabranch in the study area flows from the true right of the braidplain, where the banks are vegetated with crack willow (*Salix fragilis*) toward the true left. The actual study reach is unvegetated and composed of unconsolidated sand and gravel. Subsurface grain size distributions were estimated from four volumetric bulk samples in which the largest particle in the subsurface layer did not exceed 1% of the sample weight [*Church et al.*, 1987]. Total sample weights ranged between 176 and 395 kg. The depth of each sample hole was determined by estimating the thickness of the most recently deposited sediment layer. Grain size distributions, with associated standard deviations from the four samples, are characterized by $D_{16} = 0.84 \pm 0.15$ mm, $D_{50} = 7.5 \pm 1.6$ mm, $D_{84} = 27.9 \pm 9.7$ mm, and $D_{90} = 40.5 \pm 21.9$ mm (where D_{16}, D_{50}, D_{84}, and D_{90} represent the percentiles of the grain size distribution by mass). Surface grain size distributions were also sampled, using the standard grid-counting technique, analogous to standard *Wolman*'s [1954] pebble counts. Grain size distributions, with associated standard deviations from the 28 samples (2800 particles), are characterized by $D_{16} = 10.4 \pm 5.0$ mm, $D_{50} = 19.9 \pm 10.4$ mm, and $D_{84} = 35.2 \pm 19.2$ mm. Dead wood was deposited on bar tops, but there was no significant woody debris in the active anabranches. Given the ongoing morphological change during the study period, detailed descriptions of the braid bar unit configuration at the time of each survey are left to the Results section. During the 2010–2011 hydrological years, mean discharge at Invincible (8 km upstream from the study site) was 20 $m^3 s^{-1}$. The three maximum flows during this period were 407, 419, and 475 $m^3 s^{-1}$. Flow peaks for the same high-flow events in the adjacent Dart catchment were all greater than the Dart's mean annual maximum flow, based upon the 1997–2011 record.

3. Methodology

Five surveys of the study area were undertaken between 29 January and 2 March 2011, during a sequence of high-flow events (Figure 1c). Survey A was undertaken on the falling limb of a high-flow event that peaked

Table 1. Timing, Duration, and Flow Conditions for Each aDcp Survey[a]

Survey	Time and Date	Duration of Survey (h)	Invincible Gauge Discharge ($m^3 s^{-1}$)[b]			Time Elapsed Between Previous High-Flow Peak Discharge and Start of Survey (h)
			Start of Survey	End of Survey	Difference During Survey	
A	09:31, 29 January 2011	3	22	19	−3	7
B	16:00, 7 February 2011	3	75	70	−4	17
C	07:35, 10 February 2011	3.5	40	40	+0	81
D	17:10, 16 February 2011	3	20	21	+1	234
E	16:29, 2 March 2011	3.5	39	30	−9	11

[a]The Invincible gauging station was located 8 km upstream of the study area, where the Rees River is confined in a bedrock gorge.
[b]Not all flow was routed through the braid-bar unit during all surveys due to the presence of additional anabranches on the braidplain.

at 54 $m^3 s^{-1}$. Surveys B, C, and D were all undertaken on the falling limb of one 475 $m^3 s^{-1}$ flow event. This event had the highest recorded discharge in the 18 month long (September 2009–March 2011) record at the upstream Invincible gauge. The same event produced the highest discharge recorded (1997–2011) in the adjacent Dart River catchment, which has a hydrological response similar to the Rees River. Survey E was undertaken on the falling limb of a 175 $m^3 s^{-1}$ flow event.

Table 1 lists the timing and duration of each survey. It also details the discharge at Invincible at the start and end of each survey and the time elapsed since the previous peak flow event. Flows remained relatively steady during surveys A, C, and D. However, flow at Invincible fell by 4 $m^3 s^{-1}$ and 9 $m^3 s^{-1}$ during surveys B and E, respectively. This was unavoidable because the aDcp survey required several hours to complete, and both these surveys were undertaken on the falling limb shortly after peak flows. Bed elevation, depth, and velocity measurements from aDcp samples acquired during surveys B, C, and D have been used to calibrate hydraulic model simulations of braided river flow [*Williams et al.*, 2013] but have not previously been utilized to map flow pattern, v_a, and morphological change.

Figure 2 shows an overview of the data acquisition and postprocessing strategy. Each survey involved the deployment of (i) an aDcp to map depth, depth-averaged velocity, and v_a and (ii) a terrestrial laser scanner to survey exposed topography. The steps involved in acquiring and postprocessing survey data are outlined below.

3.1. aDcp Survey

Acoustic surveys were undertaken with either a Sontek S5 (survey A) or M9 (surveys B, C, D, and E) RiverSurveyor mounted on a Sontek hydroboard or Oceanscience Riverboat trimaran, respectively. Due to the shallow-flow conditions, both RiverSurveyor instruments used four 3 MHz transducers for water velocities and bottom tracking. The S5 is equipped with a 1.0 MHz vertical beam transducer, while the equivalent transducer on the M9 operates at 0.5 MHz. For each survey, the RiverSurveyor platform was tethered at the bow with two ropes. Operators standing on opposite banks maneuvered the platform along zigzag transects, with a nominal 1–2 m streamwise spacing. The platform was moved at a speed lower than the mean water velocity. A GPS antenna was mounted on the platform, with positioning of the S5 supported by a Leica 1200 Real Time Kinematic (RTK)-GPS unit, while the M9 positioning fix was obtained using a Novatel RTK-GPS. Position corrections were received in real time from a base station and delivered directly to the RiverSurveyor system, facilitating centimeter-scale, three-dimensional positional accuracy. Measurements of water surface elevation, depth, and 0.1 m vertical bins of velocity in the x and y directions were acquired in 1 Hz ensembles based on higher-frequency, 10 Hz sampling. Due to aDcp submergence and blanking distance, a minimum water depth of 0.4 m was required to record water velocity, and the top of the first water velocity bin was at 0.2 m below the water surface. Bottom-track velocities and RTK-GPS positions were recorded concurrently at the same frequency. Bottom-track velocities were recorded in water depths as low as 0.23 m, which is the limit of measuring depth using the S5. For surveys B, C, and D, an RTK-GPS survey of the water edge was undertaken. This enabled a comparison between the extent of total wetted area and the extent of the aDcp survey. Results show that the extent of the aDcp survey represented 69%, 63%, and 70% of the total inundated area for surveys B, C, and D, respectively.

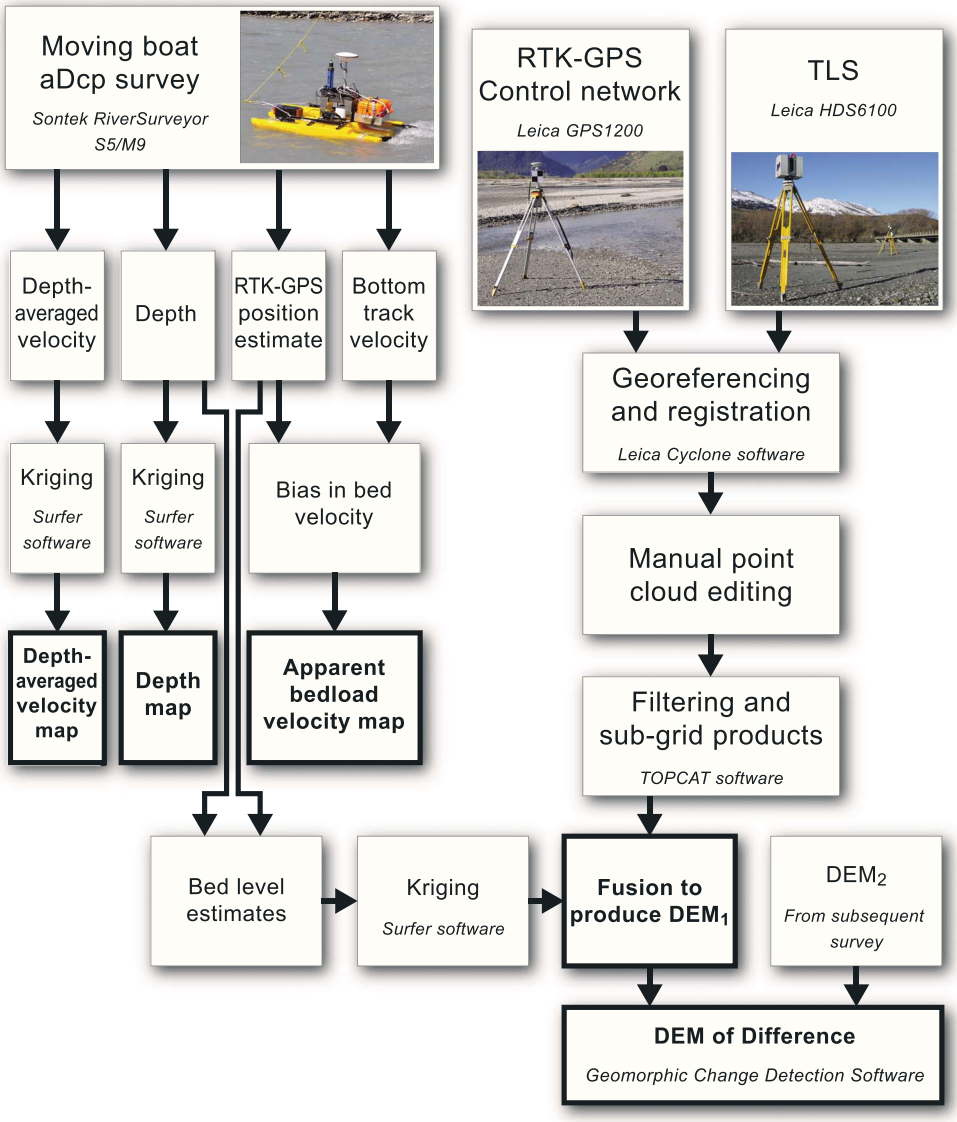

Figure 2. Data acquisition and processing workflow for each survey. TLS workflow is based on *Williams et al.* [2014].

3.2. Depth, Velocity, and Apparent Bed Load Velocity Mapping

Depth and depth-averaged velocity measurements were plotted using RTK-GPS for positions and boat velocities, rather than bottom tracking, due to the mobile bed conditions that were observed during each survey. Bottom track depth measurements were plotted in preference to vertical beam depth measurements as this metric averages samples from the four 3 MHz transducers and so smoothes bed irregularities and roughness. The four transducers are configured at a 25° angle from vertical, with 90° spacing between one another. This results in the diameter of sampling at the bed being approximately equal to the depth. Bottom track depth measurements were first corrected for the attitude of the boat [*Rennie et al.*, 2002] which is also logged at 1 Hz. Depth was then interpolated using ordinary kriging, adopting the same method as *Rennie and Millar* [2004]. Anisotropic model variograms were fitted to empirical variograms, and gridding was undertaken at a 2 m resolution, consistent with the streamwise transect spacing and sample density.

Depth-averaged water velocities, U, were calculated for each measured profile [see *Rennie and Church*, 2010] and then interpolated using the same approach applied to depth measurements. The primary anabranch had a streamwise flow direction that closely followed cardinal direction, so interpolation was undertaken

in north and east directions for the primary and secondary flow components. Velocity magnitude was calculated by taking the square root of the sum of the squared velocities in the north and east directions.

Apparent bed load velocity, v_a, was determined from the vector difference between boat velocity estimated from bottom tracking, v_{BT}, and boat velocity estimated from the actual boat track, $v_{RTK\text{-}GPS}$ [*Rennie et al.*, 2002]:

$$v_a = v_{RTK\text{-}GPS} - v_{BT} \tag{1}$$

The vectors were then interpolated using ordinary kriging for the easterly and northerly components, using the same procedure applied to depth-averaged velocity.

Zones of statistically significant v_a were identified using the method outlined in *Rennie and Church* [2010], adapted for the four-beam M9 transducer configuration. First, a compound Poisson gamma (CPG) signal plus noise model [*Rennie and Millar*, 2007] was fitted to the observed probability density function of a v_a time series acquired from a stationary boat positioned in the study area main anabranch on 23 February 2011. The CPG distribution developed in *Rennie and Millar* [2007] describes the distribution of bed load particle velocities, spatially averaged within the insonified bottom track beam footprint. It assumes that bed load transport is a stochastic phenomenon that is best described by a Poisson process and the distribution of bed load particle velocities follows a gamma probability distribution. *Rennie and Millar* [2007] presented a method that, while considering beam geometry, estimates the actual bed load velocity CPG by fitting a convolution of the estimated CPG signal and Gaussian measurement noise distributions to the observed distribution of a v_a time series. The mean and standard deviation of the streamwise component of v_a during this 1.8 h time series were, respectively, 0.081 m s^{-1} and 0.191 m s^{-1}. A good fit was achieved with the convolution technique, and the estimated CPG model parameters for particle velocity mean ($v_p = 0.22$ m s^{-1}) and standard deviation ($\sigma_{vp} = 1.72$ m s^{-1}) were similar to those estimated for the Fraser River [*Rennie and Church*, 2010]. This CPG model was used to estimate the real temporal variability in v_a, assuming that the measured v_a magnitude for each sample in the spatial distributions represented the local mean. The magnitude of v_a was utilized instead of the streamwise component because water velocity data were often not available in shallow areas for the calculation of streamwise direction.

Sampling errors were also estimated. These arise from bottom tracking, compass, and RTK-GPS measurement errors. Bottom track error velocity (v_e) was used to estimate bottom-track errors for each ensemble, accounting for both acoustic noise and heterogeneous bed load velocities between the four-beam sampling areas [see *Rennie and Church*, 2010]. Sontek reports the difference in two measurements of bottom track vertical velocity (v_{z1} and v_{z2}) from independent beam pairs as the "difference velocity" (v_d). This difference velocity should be

$$v_d = v_{z1} - v_{z2} = \frac{-b_2 - b_4}{2\cos\theta} - \frac{-b_1 - b_3}{2\cos\theta} = \frac{b_1 - b_2 + b_3 - b_4}{2\cos\theta} \tag{2}$$

where b_i represents a bottom track beam velocity. However, v_d reported by Sontek is half this value (D. Mueller, personal communication, 2013, and confirmed by the authors). Furthermore, the vertical velocity difference can be converted to a horizontal velocity error (v_e) using the following transform [*Teledyne RD Instruments*, 2010]:

$$v_e = \frac{b_1 - b_2 + b_3 - b_4}{2\sqrt{2}\sin\theta} \tag{3}$$

Thus, v_e was calculated from reported v_d by multiplying by a factor of $2^{0.5}\cot\theta = 3.03$. The compass error for the calibrated RiverSurveyor compass was assumed to be 2° [*Marsden*, 2012], and the resulting error in bottom-track velocity was calculated for every ensemble using equation (A7) of *Rennie and Church* [2010]. The error in RTK-GPS-derived velocity was assumed to be 0.031 m s^{-1} [*Rennie and Rainville*, 2006]. Finally, the total uncertainty due to both bed load temporal variability and measurement errors was calculated using the root sum of squares [*Rennie and Church*, 2010, equation (A6)]. Similar to the findings of *Rennie and Church* [2010], total uncertainty was dominated by estimated temporal variability of bed load, and uncertainty of v_a maps was large due to both total uncertainty of individual v_a estimates and the interpolation procedure (Table 2). The particularly high uncertainty in the Rees River data was due to the large observed apparent bed

Table 2. Summary of Apparent Bed Load Velocity Mean Statistics for Measurements and Error Model[a]

Survey	v_{a_prim} ($m\,s^{-1}$)	σ_{va_prim} ($m\,s^{-1}$)	v_{a_mag} ($m\,s^{-1}$)	σ_{va_mag} ($m\,s^{-1}$)	σ_{bl} ($m\,s^{-1}$)	σ_{bs} ($m\,s^{-1}$)	σ_{kb} ($m\,s^{-1}$)
A	0.126	0.271	0.300	0.222	0.239	0.262	0.340
B	0.202	0.459	0.484	0.339	0.293	0.330	0.486
C	0.107	0.353	0.363	0.283	0.261	0.286	0.391
D	0.112	0.338	0.315	0.300	0.246	0262	0.372
E	0.219	0.416	0.427	0.293	0.292	0.332	0.400

[a] v_{a_prim} is the mean single ensemble apparent bed load velocity resolved in the streamwise direction, v_{a_mag} and σ_{va_mag} are the mean and standard deviation of single ensemble apparent bed load velocity magnitude, σ_{bl} is the mean uncertainty of v_a due to real bed load temporal variability, σ_{bs} is the mean total uncertainty of v_a, and σ_{kb} is the uncertainty of v_a mapping as represented by the mean of v_a kriging standard deviation magnitudes.

load velocities, which resulted in large uncertainty due to real temporal variability of bed load. As will be seen below, the mean values of v_a are resolved in the primary streamwise direction (v_{a_prim}) for five different Rees River surveys that ranged from 0.11 to 0.22 $m\,s^{-1}$, whereas during two different surveys on the Fraser River [*Rennie and Church*, 2010], v_{a_prim} was only 0.06 $m\,s^{-1}$. Regardless, for each Rees River survey, it was possible to identify and map locations within the study area where relatively high bed load occurred and there was 87% confidence that v_a was greater than zero.

3.3. TLS Survey

Exposed braidplain topography was surveyed using a Leica HDS6100 phase-based terrestrial laser scanner. Scanning procedures were similar to those reported by *Williams et al.* [2014] except that the scanner wasmounted on a tripod rather than a vehicle. Between 14 and 20, scans were acquired of the braid bar unit during each survey. Scan stations were located at anabranch edges, or on midchannel bars, and positioned to maximize survey point density and minimize any shadow effects from banks, following standard scanning guidance [*Heritage and Hetherington*, 2007]. The maximum spacing between scan stations was 50 m and typically acquired a cloud of 10 to 15 million points. A floating control network was provided by two highly reflective targets positioned 10 to 15 m from the scanner at an angle of 120° to one another. The targets were positioned using a Leica 1200 GPS employing RTK processing until a minimum three-dimensional point quality of 15 mm was achieved. The mean point quality from targets across all surveys was 10 mm.

3.4. DEM Construction

A DEM for each survey was constructed by first processing inundated bed level aDcp data and then processing exposed braidplain TLS data. The bed level aDcp data were interpolated using ordinary kriging, mirroring the approach for mapping the hydraulic variables. Gridded data were resampled to point data, for use in subsequent data fusion. TLS data were processed using the methodology developed by *Williams et al.* [2014]. In brief, each point cloud was first georeferenced to the New Zealand Transverse Mercator Projection using a resection from pairs of RTK-GPS-derived target locations. Georeferenced point clouds were then unified into a single point cloud, decimated to a quasi-uniform point spacing of 0.02 m, edited to remove survey artifacts and objects, and filtered spatially (using TOPCAT software [*Brasington et al.*, 2012]) at 0.25 m resolution to yield precise coordinates of the minimum elevation in each 0.25 m cell. The aDcp bed level and exposed braidplain TLS data sets were fused together using Delaunay triangulation, with breaklines along channel edges, and resampled to a 0.25 m resolution.

3.5. DEM Differencing

DEM differencing techniques were used to map the spatial distribution of erosion and deposition between surveys. Probabilistic thresholding was used to distinguish between real geomorphic change and model noise [*Brasington et al.*, 2003]. By assuming that errors associated with two DEMs were approximated by the standard deviation error (SDE), the critical threshold error, U_{crit}, is

$$U_{crit} = t\sqrt{SDE^2_{DEM1} + SDE^2_{DEM2}} \quad (4)$$

Table 3. Summary of Maximum, Mean, and Root-Mean-Square Error (RMSE) Statistics From Each Spatially Variable Standard Deviation Grid Associated With Bed Level Elevation Kriging

Survey	Maximum (m)	Mean (m)	RMSE (m)
A	0.096	0.050	0.051
B	0.110	0.046	0.049
C	0.144	0.036	0.039
D	0.056	0.025	0.026
E	0.055	0.025	0.026

where t is the two-tailed Student's t distribution for the 87% confidence interval. The 87% confidence interval is consistent with that used to map statistically significant v_a. Spatially constant values of the SDE were estimated for the TLS and aDcp bed level surveys by considering the dominant errors associated with the elevation data acquired using each technique. Uncertainty in the TLS-derived DEM was assumed to be a function of surface roughness, using the D_{90} grain size of 40.5 mm. This assumption is based upon the low errors associated with TLS survey relative to the microtopography of the braidplain. Errors in the aDcp-derived bathymetry were mapped using grids of spatially variable standard deviations from kriging (Table 3). Although errors in depth measurements and RTK-GPS vertical elevation estimates also contribute to errors in estimated bed levels, the kriging standard deviations were considered to be the dominant source of error. Kriging errors were highest for surveys where there were patches with no aDcp measurements due to difficulties in manipulating the tethered boats at high flow.

4. Results and Interpretation of Bar-Scale Kinetics

The objective of this section is to describe the evolution of the study area during the monitoring period. Emphasis is placed on the links that can be inferred between morphological change and distributions of water velocity and apparent bed load velocity. A set of figures shows the sequence of surveys adjacent to one another to aid cross comparison between surveys and variables. Figure 3 shows maps of U and v_a for each survey. Zones of statistically significant v_a, at the 87% confidence interval, are identified on the v_a maps. Figure 4 shows the DEMs that were acquired after each aDcp survey and the resulting thresholded DoDs. Figure 5 schematizes the observations from each of the five surveys. Several supporting figures show further information to aid the result's interpretation. Figure S1 in the supporting information shows maps of aDcp observations and depth, while Figure S2 in the supporting information displays oblique photos that reveal the evolution of the upper study area.

4.1. Survey A

Survey A was conducted on the falling limb of a 54 $m^3 s^{-1}$ flow event (Figure 1c). Discharge at Invincible was 22 $m^3 s^{-1}$ at the start of the survey (Table 1). Flow was concentrated in the main anabranch at the upstream end of the study area, where the highest velocity (A1 in Figure 3a) and depth (Figure S1f in the supporting information) were on the channel true left. Some of this flow diverged into a minor anabranch at a diffluence in the lower portion of the study reach (A2 in Figure 3a). This minor anabranch included a confluence with another channel (A3 in Figure 3a), with a 1.1 m deep scour hole (A4 in Figure 3a). During fieldwork, a shear layer was evident at the interface between the converging flows. Maximum flow velocities observed during survey A were approximately 1.9 m s^{-1} and were associated with deeper channel locations.

The v_a map (Figure 3f; schematized in Figure 5) identified a significant bed load pathway on the true left side of the main anabranch, at the upstream end of the study area. This pathway was evident along the true left of the main anabranch farther downstream, although the statistically significant zones were not continuous. At the diffluence, where flow diverges into a minor anabranch, a significant bed load pathway was identified along the minor anabranch. This suggests that bed material was being transported into the minor anabranch. Significant v_a was also evident along the minor anabranch that joined at the scour hole.

4.2. Survey B

After survey A, four high-flow events occurred (Figure 1c). Survey B was acquired at a discharge of 75 $m^3 s^{-1}$ (Table 1), during the falling limb of a 475 $m^3 s^{-1}$ high-flow event that inundated the entire braidplain. Considerable morphological change was evident (Figure 4f; schematized in Figure 5) due to the series of high-flow events that occurred between surveys A and B. This was reflected by the small area below the estimated U_{crit} (i.e., 84% of the compared area was above the U_{crit}). At the upstream end of the study area,

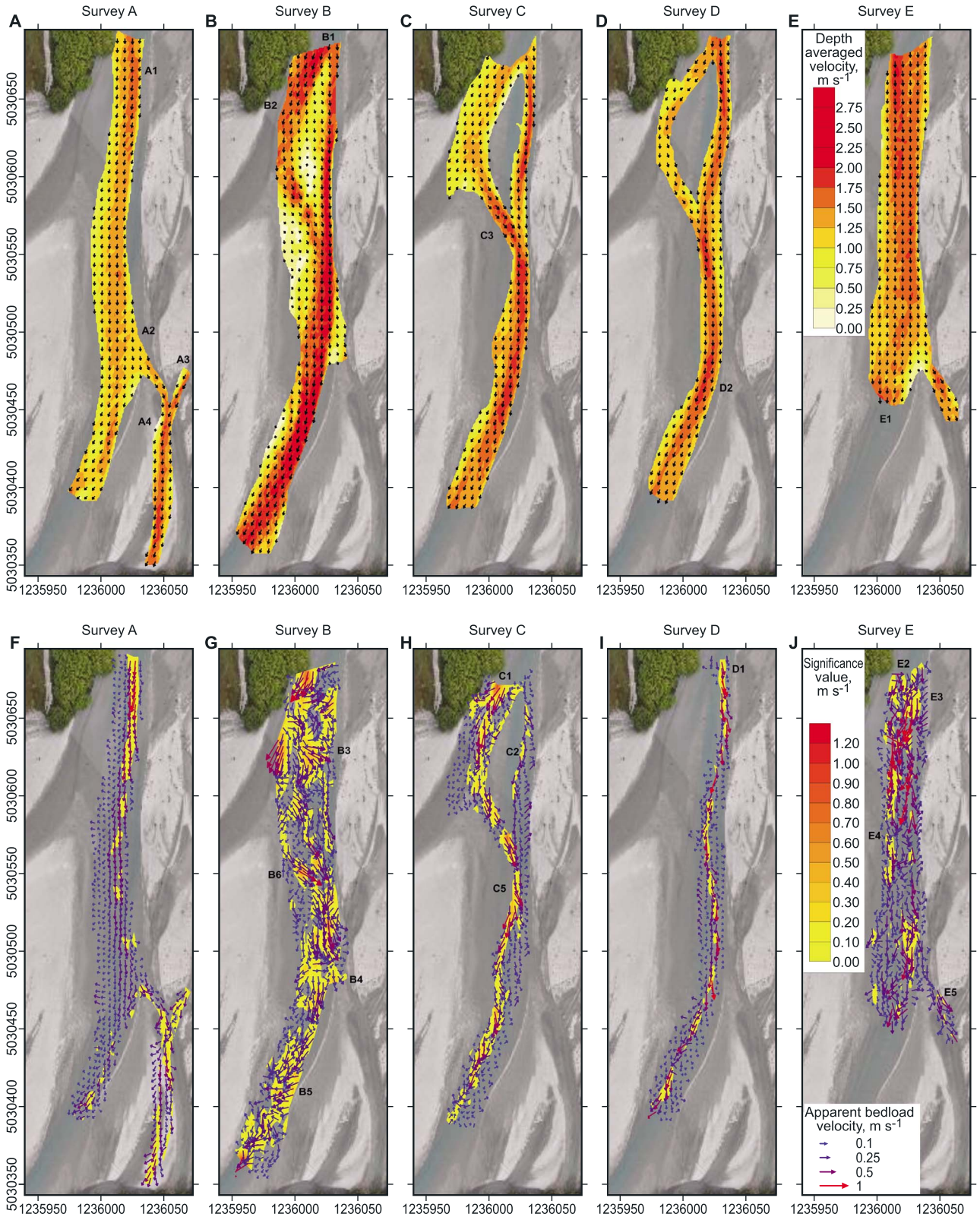

Figure 3. (a–e) Interpolated depth-averaged velocity and (f–j) apparent bed load velocity for each survey. Both depth-averaged velocity and apparent bed load velocity maps show vectors for every second grid cell. The significance value raster identifies locations of statistically significant apparent bed load velocity, where there was an 87% confidence that v_a was greater than zero. The reported significance value is $v_a - 1.5 \times \sigma_{bs}$. The same aerial image, acquired between surveys D and E, is used as a background for each map. The numbered locations marked on the figures are referred to in the article. The coordinate grid is in New Zealand Transverse Mercator.

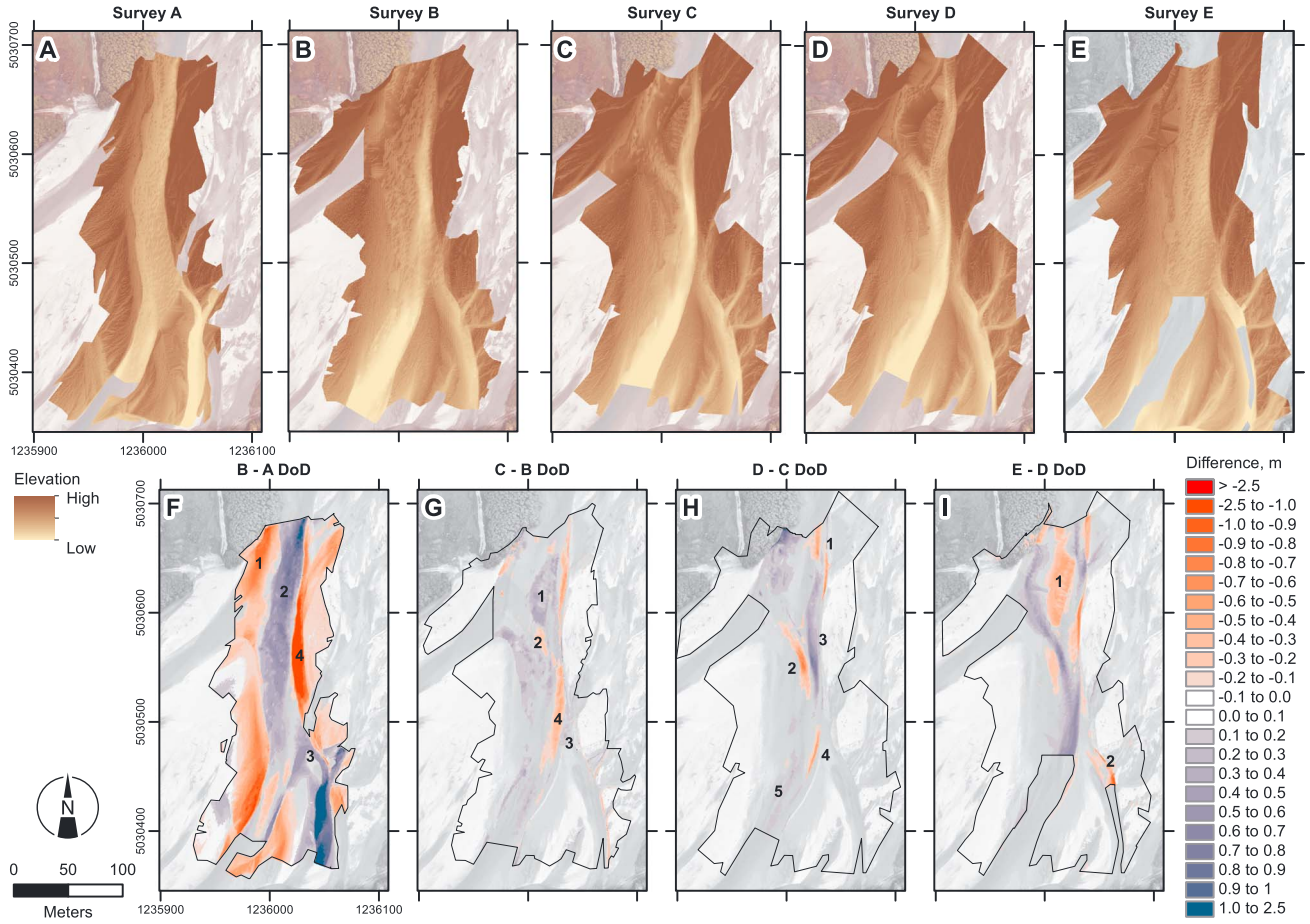

Figure 4. (a–e) DEMs for each survey and (f–i) calculated DEMs of Difference (DoD). DoDs are calculated using a probabilistic framework and show significant change at the 87% confidence interval. The same aerial image, acquired between surveys D and E, is used as a background for each map. The numbered locations marked in Figures 4f–4i are referred to in the article. The coordinate grid is in New Zealand Transverse Mercator.

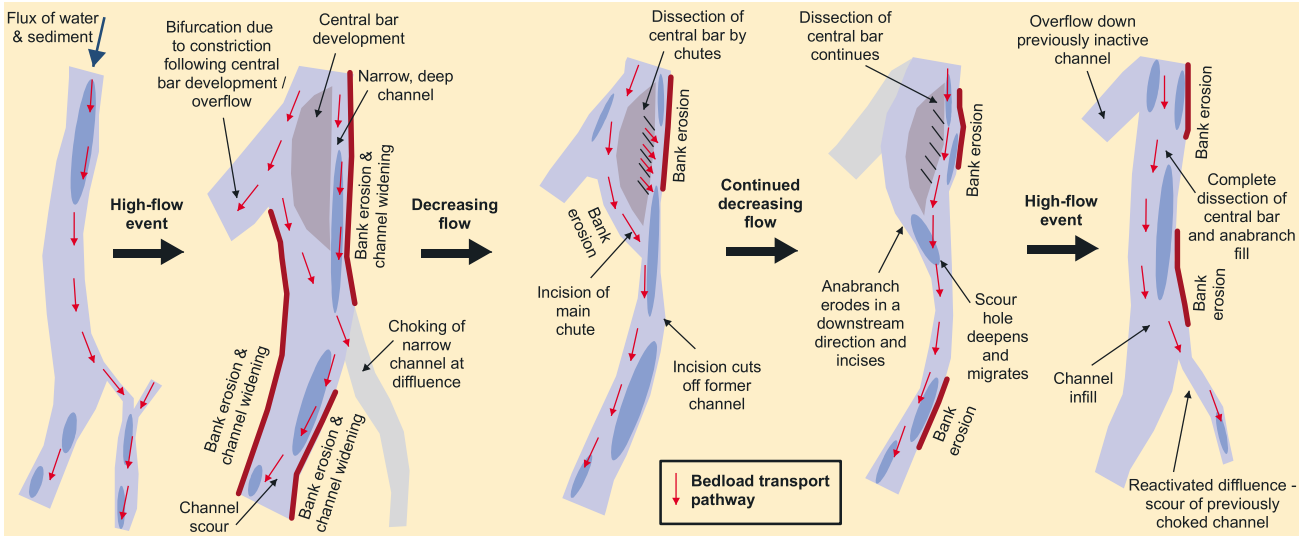

Figure 5. Diagram showing key channel features and their evolution during the monitoring period. The red arrows show major observed apparent bed load pathways. Not to scale.

there was considerable erosion of the transverse bar on the true right (1 in Figure 4f). The main anabranch that was measured in survey A filled with sediment (2 in Figure 4f) and a central bar was formed. The v_a map showed a significant flux of sediment into the study area from the true right. This was likely to be indicative of bed load flux during the high-flow events prior to survey; inflowing sediment stalled and a positive feedback loop then developed between lateral flow expansion and bar accretion due to a loss of flow competence. Central bar formation in braided rivers was described by *Ferguson* [1993] as a principal mechanism of channel change and evolution; it was also previously identified by *Leopold and Wolman* [1957] and *Ashmore* [1991]. The formation of the central bar forced flow to bifurcate (B1 in Figure 3b) at the upstream end of the study area. Further downstream, flow diverged into a minor anabranch on the true right, just downstream of the willow trees at the top of the study area (B2 in Figure 3b). This channel was not surveyed because flow depths were less than the detection limits of the aDcp.

Compared to survey A, the v_a magnitudes in survey B were higher. In addition to the connection between bed load transport flux into the study area and central bar development, several further links were evident. First, vectors indicate transport from true right to left across the submerged central bar, which was associated with the development of a submerged chute (B3 in Figure 3g; schematized in Figure 5). Second, downstream of the confluence, there were high vectors on the true left that indicated a bed load path toward the minor anabranch that was identified, and measured, during survey A (B4 in Figure 3g). This minor anabranch was filled with sediment, to depth of approximately 1 m (3 in Figure 4f), between surveys A and B. It is proposed that the bed load transport pathway into this anabranch, which was observed in survey A, continued during the high-flow events and consequently filled up and effectively choked off this anabranch. The source of material was likely to have been from bank erosion immediately upstream (4 in Figure 4f). This was associated with the constriction of the anabranch following central bar development, resulting in high shear stresses along this channel.

The correspondence between the thalweg, zones of greatest hydraulic forcing, and v_a distribution was variable. Along the main anabranch, toward the downstream end of the study area, v_a approximately followed the thalweg, and lines of highest depth and velocity, moving from the true left to the true right (B5 in Figure 3g). However, along the flow path on the true right of the central bar, the bed load vectors were higher to the true right of this flow path than they were within the flow path itself (B6 in Figure 3g).

4.3. Survey C

Survey C was undertaken 3 days after survey B, on the falling limb on the same high-flow event. At the start of the survey, the discharge at Invincible was 40 $m^3 s^{-1}$ (Table 1), considerably lower than survey B. The DoD between surveys B and C showed significant erosion and deposition in a number of areas (Figure 4g). Morphological change was less extensive than observed between surveys A and B, but the patterns were coherent and indicate that morphological activity continued during the event recession even though flows were relatively moderate (in this case 20% of the compared braidplain was above the U_{crit}). Areas that were identified with significant v_a (Figure 3h) suggest that there was a flux of bed material into the study area along the true right anabranch (C1 in Figure 3h; schematized in Figure 5). The elevation of the central bar continued to increase between surveys B and C (1 in Figure 4g). It is proposed that flow across the bar diverged and decelerated, thus causing bed load to stall, resulting in deposition. Subsequently, as flow receded, the hydraulic gradient between the true right and left anabranches around the bar caused multiple chutes to form, dissecting [*Ferguson*, 1993] the bar surface (Figure S2c in the supporting information). Areas of significant v_a were detected on the true left side of the bar (C2 in Figure 3h). These areas correspond to confluences between chutes dissecting the bar and the narrow anabranch. In the field, small submerged fans were observed at these confluences.

Further downstream, the primary pathway for bed load was around the true right of the central bar and then down a steep chute (C3 in Figure 3c). The confluence of this chute with the main anabranch was characterized by the highest observed flow velocity of approximately 2.0 m s^{-1}. A dominant pathway appears to be associated with not only upstream sediment supply but also bar head erosion (2 in Figure 4g). This is important, since it appears that a switch occurred during the 475 $m^3 s^{-1}$ event recession that changed head over the central bar, resulting in different flow acceleration into banks, thus altering the location of bank erosion. Downstream of the central bar, the bed load pathway was along the true right of the main anabranch. Significantly, this pathway was not through the deepest (approximately 1.2 m) section of the

confluence scour hole (C4 in Figure S1h in the supporting information) and was not coincident with the main anabranch's thalweg. The significant v_a pathline does turn toward the true left at the point where the minor anabranch was choked between surveys A and B (C5 in Figure 3h). This indicates that some materials may have deposited toward the true left of the anabranch (3 in Figure 4g), continuing the process of choking. Expansion of the primary anabranch was also observed (4 in Figure 4g).

4.4. Survey D

Survey D was conducted 6 days after survey C. At the time of survey, discharge had fallen to 21 $m^3 s^{-1}$ (Table 1) and the central bar was aerially exposed (Figure S2d in the supporting information). The map of v_a for survey D is missing data for the anabranch to the true right of the midchannel bar. This was due to the loss of RTK-GPS lock, and a resulting degradation of three-dimensional position estimates, for this component of the survey. While patterns of depth-averaged velocity and depth could still be interpolated, the position estimates were not resolved with sufficient accuracy to estimate v_a. Importantly, however, transects across the full width of the channel upstream of the diffluence around the bar were obtained. These transects showed significant v_a on the true left of the channel (D1 in Figure 3i). This sediment supply was likely to be linked to bank erosion (1 in Figure 4h). It was notable that this bed load transport pathway was along the channel to the true left of the bar, whereas for survey C, a pathway was not observed on this side of the bar except for the formation of fans from minor chute channels (schematized in Figure 5). The bed load pathway was coherent along the entire length of the surveyed anabranch and approximately followed the thalweg. At the confluence, at the downstream end of the central bar, significant v_a vectors remained to the true left of the shear layer and an input of bed load was not identified from the true right.

The morphological evolution of the confluence at the downstream end of the central bar was particularly striking. The scour hole at the confluence migrated laterally toward the true right between surveys C and D (2 in Figure 4h). This lateral migration accounts for a high proportion of the morphological activity observed during relatively low-flow conditions. The migration was likely a consequence of the relatively steep gradient along the true right anabranch upstream of the confluence. The scour hole was also reorientated to align with the maximum velocity vectors of this anabranch. Downstream of the confluence, on the true right of the channel, low-magnitude bar accretion was observed (3 in Figure 4h), which was likely a response to sediment scoured from the confluence. The reorientation of the scour hole caused changes in the near left-bank flow field, causing bank erosion (4 in Figure 4h) at a location where flow velocities were highest against the bank (D2 in Figure 3i). Significant v_a vectors tracked the transport of this sediment toward the true right, following the line of maximum velocity vectors, to a zone of deposition (5 in Figure 4h).

4.5. Survey E

Between surveys D and E, there were two high-flow events with peaks of 92 and 175 $m^3 s^{-1}$. It was upon the falling limb of this latter high-flow event that survey E was acquired, when discharge was 39 $m^3 s^{-1}$ (Table 1). Survey E shows that flow was predominantly constrained to one major anabranch at the upstream end of the study area, although some flow did bifurcate to the true right in the same position as the bifurcation at the bar head observed in surveys B, C, and D. However, flow toward the true right was shallow and below the aDcp detection limit, as shown in Figure 3e. Flow was also shallow in the main anabranch toward the downstream end of the study area (E1 in Figure 3e), resulting in a shorter surveyed section than in the previous surveys.

The high-flow events between surveys D and E caused considerable morphological change within the study reach (Figure 4i; schematized in Figure 5), resulting in flow paths and patterns that are distinct from those observed during survey D. The process of bar dissection that was noted in surveys C and D continued during the higher flows between surveys D and E resulting in complete erosion of the central bar (1 in Figure 4i), illustrating a cycle of sediment deposition and subsequent erosion during the monitoring period. The v_a map indicated a sediment flux from upstream of the study area (E2 in Figure 3j). Bed load speeds were relatively high in the region where flow converged from either side of the main anabranch (E3 in Figure 3j). The significant bed load pathway was then predominantly along the true right of the main anabranch (E4 in Figure 3j), adjacent to the zone of erosion along the true left of the former central bar.

In survey E, the bifurcation toward the downstream end of the study area was observed to have reactivated; thus, a complete choking/reactivation cycle was observed during the monitoring period. The secondary

anabranch was reactivated during the high flows that occur between surveys D and E due to deposition in the primary anabranch. This caused the water level in the primary anabranch to rise. Flow then spilled over the outside of the bend into the secondary anabranch. Overflowing water scoured the secondary anabranch, causing headward incision and the capture of further flow. The v_a vectors upstream of this diffluence indicated that sediment was not being transported into the minor anabranch. Within this anabranch (E5 in Figure 3j), there was a zone of significant transport located on the true left of the channel. Since the DoD indicates that the true left bank of this anabranch eroded between surveys D and E (2 in Figure 4i), this bank was likely to be connected to the initiation of this bed load transport pathway. Overall, the erosion of the central bar and the reactivation of the downstream bifurcation result in a configuration of anabranches during survey E that was very similar to that measured during survey A.

5. Discussion

5.1. Connecting Bed Load Transport to Morphological Change and Flow Dynamics

A number of braiding mechanisms are evident from the DoD and v_a observations reported in this paper. These include anabranch choking and reactivation, central bar development, bar dissection, scour pool migration, and bank erosion. During the monitoring period, reworking of sediment resulted in morphological changes that returned the study area to a configuration similar to that observed during the initial survey. As well as observing the morphological signatures [*Wheaton et al.*, 2013] of changes associated with particular braiding mechanisms, the v_a pathway observations provide evidence to make inferences about lateral and longitudinal connections [*Fryirs et al.*, 2007] between zones of erosion and deposition through the channel network. This is possible because v_a mapping confirms the presence of narrow bands of bed load transport [*Thompson*, 1985; *Gomez*, 1991; *Ferguson et al.*, 1992; *Warburton*, 1992]. This mapping shows that pathways between zones of erosion and deposition were typically relatively short, i.e., from an upstream source to the nearest downstream sink. Recent small-scale laboratory modeling of braided river morphodynamics has utilized DoDs and fluorescent tracer particles to indicate connectivity between zones of erosion and deposition [*Kasprak et al.*, 2014]. While tracer particles were not utilized for the study presented here, the inferences that can be derived from interpreting v_a pathways between zones of erosion and deposition document aspects of braided river processes that are challenging to measure in laboratory models.

The choking and reactivation of the bifurcation toward the downstream end of the study area was one of the clearest braiding mechanisms. Moreover, the example showed the connection between sediment sources, pathways, and sinks. The v_a surveys that were undertaken during surveys A and B clearly showed a bed load pathway into the secondary anabranch. Based upon analysis of the DoD, it is proposed that bed material was supplied to this pathway by erosion that occurred immediately upstream from a bar edge. Across all the surveys, bank erosion was identified to be an important source of bed material since sediment in the study area was unconsolidated and banks were not vegetated. This observation concerning the importance of bank erosion is in line with observations made in other braided contexts [*Carson and Griffiths*, 1989; *Bertoldi et al.*, 2010; *Wheaton et al.*, 2013]. The supply of material from bank erosion is influenced by changing flow path directions and driven by changes in head through complex bar topography and the stochastic nature of the collapse of the Rees' banks.

In addition to considering connections between bed load pathways and morphological change, the data set also enables analysis of the correspondence between flow patterns and bed load transport. In all the DoDs, spatially discrete, elongated bands of bank erosion were identified on the outside of channel bends. These zones of bank erosion were coupled to the locations where high velocities, and hence high shear stresses, were mapped. Patterns of bed load transport observed during surveys that were undertaken at higher flows suggest that sediment supply was a key control on the location of bed load pathways when morphological activity was occurring at a high rate. For example, v_a mapping from surveys A, C, and E indicated that bed load transport pathways do not necessarily follow the path of greatest hydraulic forcing but neither do they cross it. In addition to these broad trends, the routing of flow and bed load through the confluence downstream of the central bar is notable since v_a mapping (survey C) indicated that the predominant bed load pathway can be routed around the scour hole at some flow stages. These dynamics around pools have also been observed by *Milan* [2013] in clast tracer studies.

Further work to analyze the correlation between bed load transport pathways and hydraulic forcing is ongoing. This work is focusing upon mapping shear stress distribution, derived from aDcp depth and depth-averaged velocity. We are also working to convert values of v_a to bed load transport rates (in units of kg m^{-1} s^{-1}) using a site-specific calibration data set (C. D. Rennie et al., in review). Together, analysis of the correlation between bed load transport pathways and hydraulic forcing, and calculation of bed load transport rates, will provide data to verify two-dimensional model predictions of shear stress and entrainment.

5.2. Monitoring Dynamics at High Flows

The fusion of aDcp- and TLS-surveying methodologies as presented in this paper has provided the means to relate the spatial distribution of bed load transport to flow patterns during high flows, in shallow gravel bed braided rivers that cannot be navigated by crewed vessels. The maximum discharge that was surveyed during the monitoring campaign was 75.0 m^3 s^{-1} (at Invincible; survey B). While this flow was below the peak of the high-flow events (Figure 1c), the data acquired during the monitoring campaign demonstrate both the efficacy of the technique and associated challenges. From a morphological perspective, while the high-flow peak was not sampled, the recession flows were morphologically competent and their prolonged duration may well have rendered them as effective at doing geomorphic work.

The concurrent acquisition of depth, flow velocity, v_a and bed topography data from tightly spaced, moving boat aDcp transects during relatively high flows was possible along the entire study reach within a few hours. Obtaining such data from direct sampling in equivalent flows would be logistically challenging. For example, *Dietrich and Smith*'s [1984] physical sampling of downstream and cross-stream bed load transport through a single meander bend required 8 days of sampling and necessitated a field site with steady, regulated flow. The v_a mapping also revealed longitudinal connections between the sediment dynamics of braided channels upstream of the study area and those downstream [*Ashmore*, 1988; *Hoey and Sutherland*, 1991]. Indeed, the direction of sediment influx into the study reach strongly influenced morphological trajectories immediately downstream.

Two issues emerge from the highest-flow survey. First, at higher flow, the feasibility of operating a tethered boat would be compromised due to a wider inundated area and higher velocities. This would not only be hazardous but the lack of control is likely to result in less spatially intensive sampling as seen in the tracks for survey B, where it is evident that there were difficulties moving the boat along evenly spaced, downstream-progressing transects during high velocities (Figure S1b in the supporting information). Consequently, if transects were less evenly spaced, kriging standard deviations would be more variable. Indeed, the kriging standard deviations obtained here were still large, owing to the high variance of measured v_a within a given survey (Table 2). The use of a remote-controlled boat as an aDcp platform could possibly overcome this difficulty, but the feasibility of using remote-controlled craft for closely spaced transect surveys in relatively high-velocity shallow rivers has yet to be established. Second, high turbidity during higher flows may obscure bottom tracking. For the sampling undertaken here, turbidity was fairly low in all but survey B, so only in survey B could v_a have been influenced by the near-bed suspended load [cf., *Rennie and Millar*, 2004]. However, the maximum values of v_a were similar in all surveys, which suggests that even in survey B, the observed v_a was likely indicative of bed load transport.

5.3. Evolution at Low Flows

Observation of morphological change and bed load transport during relatively low flows (survey D was undertaken at 20.7 m^3 s^{-1}) supports *Bertoldi et al.*'s [2010] assertion that morphological change in natural braided rivers occurs at discharges well below bankfull. Time-lapse imagery of the braided Waimakariri River indicates that at bankfull flows, morphological activity activates/creates large sheets over the interfluves between the main braids, whereas activity is confined within the main braids at lower flows [*Hicks et al.*, 2002]. Morphological activity on the Waimakariri River thus continues during low flows although at a lower rate and across a much narrower area. In contrast, in a more confined setting, *Claude et al.* [2014] note that during periods of low flow, the hydrodynamic processes that drive morphological evolution at high flows continue, albeit at a lower rate, because bar configuration and flow structure do not alter much with discharge. Across the shallow Rees River, the extent of braidplain that experiences morphological change is drastically reduced during low flows. Therefore, while the initial series of large-magnitude events are associated with channel widening, central bar formation, and

anabranch choking, during the low flows, the overall morphological configuration remains essentially the same. As such, bed load transport during low flows occurs within existing anabranches previously formed during high-flow events, with sediment supplied from locations with high bed or bank shear stress due to locally increased water surface slope at lower-flow stage. An example observed herein was the chute formation on the central bar tail during survey C. As stage diminished, flow cascaded over the bar tail, leading to high bed material entrainment and bed load transport rates. Processes such as these permit shallow braided gravel bed rivers to transport bed material even during low flows. The surveys reported here are not across the entire braidplain width, so it is not possible to consider how the spatial extent of bed load transport relates to active width [*Ashmore et al.*, 2011] at a range of flows. A monitoring campaign with full braidplain coverage, potentially with multiple boats to map v_a, would however provide an opportunity to address such questions at a large spatial scale.

6. Conclusion

The methodology presented in this paper provides novel observations that enable inferences about the connection between spatially distributed bed load transport pathways, flow patterns, and morphological change in a shallow, gravel bed braided river during high-flow events. Moreover, the methodology enables the mapping of aspects of braided river processes that are difficult to quantify in small-scale laboratory models. The fusion of TLS and aDcp bathymetric survey data enabled the generation of high-resolution DEMs that were characterized by high vertical accuracy. DEM differencing was thus characterized by low errors, enabling the identification of morphological signatures associated with different braiding mechanisms. Moving boat aDcp surveys enabled the mapping of depth-averaged velocity, bathymetry, and apparent bed load transport for five snapshots during the series of high-flow events.

Bed load moves in laterally narrow bands. Interpretation of bed load pathway maps indicated that these bands appear to connect zones of erosion and deposition. When rates of morphological activity are relatively high, the location of these bands was strongly influenced by local sediment supply. Each survey indicated coherence between zones of erosion and deposition. For example, morphological change and bed load pathway maps suggested bank erosion and head cutting were connected to anabranch choking and transverse bar accretion. During the series of high-flow events, the study reach was shown to undergo cyclical change, including the choking and reactivation of an anabranch, and central bar deposition and dissection. At low flows, morphological activity still occurred, but it was confined to a small spatial extent and occurred at a lower rate.

The coupling of aDcp and TLS surveys contributes to developing techniques to monitor the dynamics of braided rivers during high flows. It is at these flows that rates of morphological activity are high, yet they are also the most logistically challenging to measure. The approach of apparent bed load mapping provides spatially distributed observations of bed load dynamics that cannot be obtained by direct sampling during high flow. However, at flows higher than those surveyed here, a remote-controlled boat would be a necessary alternative to tethered boat operation. The methodological and data processing workflow that is presented here to couple aDcp and TLS topographic surveys can be utilized in dynamic fluvial settings across a range of river styles. Such applications will enable the investigation of lateral and longitudinal connectivity between sediment sources, bed load transport pathways, and sediment sinks within channel networks.

Acknowledgments

Helen Reid and Eric Scott are thanked for their field assistance. Antony Smith assisted with figure production. The field campaign was funded by NERC grant NE/G005427/1 and NERC Geophysical Equipment Facility Loan 892, as well as NSERC and CFI (Canada) grants to Colin Rennie. Damia Vericat has benefited from a Ramon y Cajal Fellowship (RYC-2010-06264) during the preparation of this manuscript. Richard Williams was funded by NERC grant NE/G005427/1 during fieldwork and an Aberystwyth University Postgraduate Studentship during the preparation of this manuscript. Murray Hicks was supported by NIWA's core-funded Sustainable Water Allocation Programme. Data used to produce the results of this paper are available from the authors.

References

Ashmore, P. E. (1988), Bed load transport in braided gravel bed stream models, *Earth Surf. Processes Landforms*, *13*(8), 677–695, doi:10.1002/esp.3290130803.

Ashmore, P. E. (1991), How do gravel bed rivers braid?, *Can. J. Earth Sci.*, *28*(3), 326–341.

Ashmore, P. E. (2013), Morphology and dynamics of braided rivers, in *Fluvial Geomorphology, Treatise on Geomorphology*, edited by E. Wohl, pp. 289–312, Academic Press, San Diego, Calif., doi:10.1016/B978-0-12-374739-6.00242-6.

Ashmore, P. E., and J. T. Gardner (2008), Unconfined confluences in braided rivers, in *River Confluences, Tributaries, and the Fluvial Network*, edited by S. P. Rice, A. G. Roy, and B. L. Rhoads, pp. 119–147, John Wiley, Chichester, U. K., doi:10.1002/9780470760383.ch7.

Ashmore, P. E., and E. Sauks (2006), Prediction of discharge from water surface width in a braided river with implications for at-a-station hydraulic geometry, *Water Resour. Res.*, *42*, W03406, doi:10.1029/2005WR003993.

Ashmore, P. E., W. Bertoldi, and J. T. Gardner (2011), Active width of gravel bed braided rivers, *Earth Surf. Processes Landforms*, *36*(11), 1510–1521, doi:10.1002/esp.2182.

Barton, J. S., J. Gaskin, S. A. Pittman, and C. D. Rennie (2010), Surrogate technologies for monitoring bed load transport in rivers, in *Sedimentology of Aqueous Systems*, edited by J. R. Gray and J. W. Gartner, pp. 46–79, Wiley Blackwell, Oxford, U. K.

Bertoldi, W., L. Zanoni, and M. Tubino (2010), Assessment of morphological changes induced by flow and flood pulses in a gravel bed braided river: The Tagliamento River (Italy), *Geomorphology*, *114*(3), 348–360.
Brasington, J. (2010), From grain to floodplain: Hyperscale models of braided rivers, *J. Hydraul. Res.*, *48*(4), 52–53.
Brasington, J., B. T. Rumsby, and R. A. McVey (2000), Monitoring and modeling morphological change in a braided gravel bed river using high-resolution GPS-based survey, *Earth Surf. Processes Landforms*, *25*(9), 973–990, doi:10.1002/1096-9837(200008)25:9<973::AID-ESP111>3.0.CO;2-Y.
Brasington, J., J. Langham, and B. Rumsby (2003), Methodological sensitivity of morphometric estimates of coarse fluvial sediment transport, *Geomorphology*, *53*(3–4), 299–316, doi:10.1016/S0169-555X(02)00320-3.
Brasington, J., D. Vericat, and I. Rychkov (2012), Modeling river bed morphology, roughness, and surface sedimentology using high-resolution terrestrial laser scanning, *Water Resour. Res.*, *48*, W11519, doi:10.1029/2012WR012223.
Bunte, K., S. Potyond, and S. R. Abt (2003), Sampler size and sampling time affect bed load transport rates and particle sizes measured with bed load traps in gravel bed streams, in *Erosion Sediment Transport Measurement in Rivers: Technological and Methodological Advances*, edited by J. Bogen, T. Fergus, and D. Walling, pp. 126–133, IAHS, Oslo, Norway.
Burtin, A., R. Cattin, L. Bollinger, J. Vergne, P. Steer, A. Robert, N. Findling, and C. Tiberi (2011), Towards the hydrologic and bed load monitoring from high-frequency seismic noise in a braided river: The "torrent de St. Pierre," French Alps, *J. Hydrol.*, *408*(1–2), 43–53, doi:10.1016/j.jhydrol.2011.07.014.
Carson, M. A., and G. A. Griffiths (1989), Gravel transport in the braided Waimakariri River: Mechanisms, measurements, and predictions, *J. Hydrol.*, *109*(3–4), 201–220.
Childers, D. (1999), *Field Comparisons of Six Pressure-Difference Bed Load Samplers in High-Energy Flow*, U.S. Geol. Surv., Vancouver, Wash.
Church, M., D. G. McLean, and J. F. Walcott (1987), River bed gravels: Sampling and analysis, in *Sediment Transport in Gravel Bed Rivers*, edited by C. R. Thorne, J. C. Bathurst, and R. D. Hey, pp. 43–88, John Wiley, Chichester, U. K.
Claude, N., S. Rodrigues, V. Bustillo, J.-G. Bréhéret, P. Tassi, and P. Jugé (2014), Interactions between flow structure and morphodynamic of bars in a channel expansion/contraction, Loire River, France, *Water Resour. Res.*, *50*, 2850–2873, doi:10.1002/2013WR015182.
Cook, S. J., D. J. Quincey, and J. Brasington (2013), Geomorphology of the Rees Valley, Otago, New Zealand, *J. Maps*, doi:10.1080/17445647.2013.863744.
Dietrich, W. E., and J. D. Smith (1984), Bed load transport in a river meander, *Water Resour. Res.*, *20*(10), 1355–1380, doi:10.1029/WR020i010p01355.
Dinehart, R. L., and J. R. Burau (2005), Averaged indicators of secondary flow in repeated acoustic Doppler current profiler crossings of bends, *Water Resour. Res.*, *41*, W09405, doi:10.1029/2005WR004050.
Entwistle, N. S., D. J. Milan, and G. L. Heritage (2010), Biotope mapping using combined lidar and acoustic Doppler profiler survey, paper presented at BHS 3rd International Symposium: Managing Consequences of a Changing Global Environment, Proceedings of the British Hydrological Society, Newcastle University, U. K., 21–23 July.
Ferguson, R. I. (1993), Understanding braiding processes in gravel bed rivers: Progress and unresolved problems, in *Braided Rivers*, edited by J. L. Best and C. S. Bristow, pp. 73–87, Geol. Soc., London.
Ferguson, R. I., P. E. Ashmore, P. J. Ashworth, C. Paola, and K. L. Prestegaard (1992), Measurements in a braided river chute and lobe: 1. Flow pattern, sediment transport, and channel change, *Water Resour. Res.*, *28*(7), 1877–1886, doi:10.1029/92WR00700.
Fryirs, K. A., G. J. Brierley, N. J. Preston, and M. Kasai (2007), Buffers, barriers, and blankets: The (dis)connectivity of catchment-scale sediment cascades, *Catena*, *70*(1), 49–67, doi:10.1016/j.catena.2006.07.007.
Gaeuman, D., and S. J. Pittman (2007), Relative contributions of sand and gravel bed load transport to acoustic Doppler bed-velocity magnitudes in the Trinity River, California, in *International Bed Load-Surrogate Monitoring Workshop*, edited by J. R. Gray, J. B. Laronne, and J. D. G. Marr, pp. 195–207, U.S. Dep. of the Inter. and U.S. Geol. Surv., Anthony Falls Lab., Minneapolis, Minn.
Garcia, C., J. B. Laronne, and M. Sala (1999), Variable source areas of bed load in a gravel bed stream, *J. Sediment. Res.*, *69*(1), 27–31, doi:10.2110/jsr.69.27.
Glysson, G. D. (1993), U.S. Geological Survey bed load sampling policy, paper presented at Proceedings-National Conference on Hydraulic Engineering, ASCE, San Francisco, Calif., 25–30 July.
Gomez, B. (1991), Bed load transport, *Earth Sci. Rev.*, *31*(2), 89–132, doi:10.1016/0012-8252(91)90017-a.
Gray, J. R., J. B. Laronne, and J. D. G. Marr (2010), *Bed Load-Surrogate Monitoring Technologies*, 38 pp., U.S. Geol. Surv., Va.
Guerrero, M., and A. Lamberti (2011), Flow field and morphology mapping using aDcp and multibeam techniques: Survey in the Po River, *J. Hydraul. Eng.-ASCE*, *137*(12), 1576–1587, doi:10.1061/(asce)hy.1943-7900.0000464.
Habersack, H. M., H. P. Nachtnebel, and J. B. Laronne (2001), The continuous measurement of bed load discharge in a large alpine gravel bed river, *J. Hydraul. Res.*, *39*(2), 125–133, doi:10.1080/00221680109499813.
Helley, E. J., and W. Smith (1971), *Development and Calibration of a Pressure-Difference Ded Load Sampler*, Water Resour. Div., U.S. Geol. Surv. Menlo Park, Calif.
Heritage, G. L., and D. J. Hetherington (2007), Towards a protocol for laser scanning in fluvial geomorphology, *Earth Surf. Processes Landforms*, *32*(1), 66–74, doi:10.1002/esp.1375.
Hicks, D. M., and B. Gomez (2005), Sediment transport, in *Tools in Fluvial Geomorphology*, edited by G. M. Kondolf and H. Piegay, pp. 425–461, Wiley, Chichester, England, doi:10.1002/0470868333.ch15.
Hicks, D. M., M. J. Duncan, J. M. Walsh, R. M. Westaway, and S. N. Lane (2002), New views of the morphodynamics of large braided rivers from high-resolution topographic surveys and time-lapse video, in *The Structure, Function, and Management Implications of Fluvial Sedimentary Systems*, edited by F. J. Dyer, M. C. Thoms, and J. M. Olley, pp. 273–380, Int. Assoc. for Hydrol. Sci., Wallingford.
Hoey, T. B., and A. J. Sutherland (1991), Channel morphology and bed load pulses in braided rivers: A laboratory study, *Earth Surf. Processes Landforms*, *16*(5), 447–462, doi:10.1002/esp.3290160506.
Holmes, R. R. (2007), Measurement of bed load transport in sand bed rivers: A look at two indirect sampling methods, in *International Bed Load-Surrogate Monitoring Workshop*, edited by J. R. Gray, J. B. Laronne, and J. D. G. Marr, pp. 236–252, U.S. Dep. of the Inter. and U.S. Geol. Surv., Anthony Falls Lab., Minneapolis, Minn.
Jacobson, A. R., R. Militello, and P. C. Baveye (2009), Development of computer-assisted virtual field trips to support multidisciplinary learning, *Comput. Educ.*, *52*(3), 571–580, doi:10.1016/j.compedu.2008.11.007.
Jamieson, E. C., C. D. Rennie, R. B. Jacobson, and R. D. Townsend (2011a), Three-dimensional flow and scour near a submerged wing dike: aDcp measurements on the Missouri River, *Water Resour. Res.*, *47*, W07544, doi:10.1029/2010WR010043.
Jamieson, E. C., C. Rennie, R. Jacobson, and R. Townsend (2011b), Evaluation of aDcp apparent bed load velocity in a large sand bed river: Moving versus stationary boat conditions, *J. Hydraul. Eng.*, *137*(9), 1064–1071, doi:10.1061/(ASCE)HY.1943-7900.0000373.

Jang, C. L., and Y. Shimizu (2005), Numerical simulation of relatively wide, shallow channels with erodible banks, *J. Hydraul. Eng.*, *131*(7), 565–575, doi:10.1061/(asce)0733-9429(2005)131:7(565).

Kasprak, A., J. M. Wheaton, P. E. Ashmore, J. W. Hensleigh, and S. Peirce (2014), The relationship between particle travel distance and channel morphology: Results from physical models of braided rivers, *J. Geophys. Res. Earth Surf.*, *120*, 55–74, doi:10.1002/2014JF003310.

Lallias-Tacon, S., F. Liébault, and H. Piégay (2014), Step by step error assessment in braided river sediment budget using airborne lidar data, *Geomorphology*, *214*, 307–323, doi:10.1016/j.geomorph.2014.02.014.

Lane, S. N., K. Richards, and J. Chandler (1995), Morphological estimation of the time-integrated bed load transport rate, *Water Resour. Res.*, *31*(3), 761–772, doi:10.1029/94WR01726.

Lane, S. N., R. M. Westaway, and D. M. Hicks (2003), Estimation of erosion and deposition volumes in a large, gravel bed, braided river using synoptic remote sensing, *Earth Surf. Processes Landforms*, *28*(3), 249–271, doi:10.1002/esp.483.

Leopold, L. B., and G. M. Wolman (1957), River channel patterns, braiding meandering and straight.

Marsden, R. (2012), Performance of several aDcp internal magnetic compasses, paper presented at Hydraulic Measurements and Experimental Methods 2012, ASCE and IAHR, Snowbird, Utah, 12–15 Aug.

Milan, D. J. (2013), Sediment routing hypothesis for pool-riffle maintenance, *Earth Surf. Processes Landforms*, *38*(14), 1623–1641, doi:10.1002/esp.3395.

Milan, D. J., G. L. Heritage, and D. Hetherington (2007), Application of a 3-D laser scanner in the assessment of erosion and deposition volumes and channel change in a proglacial river, *Earth Surf. Processes Landforms*, *32*(11), 1657–1674, doi:10.1002/esp.1592.

Mosley, M. P. (1982), Analysis of the effect of changing discharge on channel morphology and instream uses in a Braided River, Ohau River, New Zealand, *Water Resour. Res.*, *18*(4), 800–812, doi:10.1029/WR018i004p00800.

Mosley, M. P. (1983), Response of braided rivers to changing discharge, *J. Hydrol. (New Zealand)*, *22*, 18–67.

Muste, M., K. Yu, and M. Spasojevic (2004), Practical aspects of aDcp data use for quantification of mean river flow characteristics: Part 1. Moving-vessel measurements, *Flow Meas. Instrum.*, *15*(1), 1–16, doi:10.1016/j.flowmeasinst.2003.09.001.

Nicholas, A. P. (2013a), Morphodynamic modeling of rivers and floodplains, in *Fluvial Geomorphology, Treatise on Geomorphology*, edited by E. Wohl, pp. 160–179, Academic Press, San Diego, Calif., doi:10.1016/B978-0-12-374739-6.00037-3.

Nicholas, A. P. (2013b), Modeling the continuum of river channel patterns, *Earth Surf. Processes Landforms*, *38*(10), 1187–1196, doi:10.1002/esp.3431.

Nicholas, A. P. (2013c), Morphodynamic diversity of the world's largest rivers, *Geology*, *41*(4), 475–478, doi:10.1130/g34016.1.

Parsons, D. R., J. L. Best, O. Orfeo, R. J. Hardy, R. Kostaschuk, and S. N. Lane (2005), Morphology and flow fields of three-dimensional dunes, Rio Paraná, Argentina: Results from simultaneous multibeam echo sounding and acoustic Doppler current profiling, *J. Geophys. Res.*, *110*, F04S03, doi:10.1029/2004JF000231.

Parsons, D. R., J. L. Best, S. N. Lane, O. Orfeo, R. J. Hardy, and R. Kostaschuk (2007), Form roughness and the absence of secondary flow in a large confluence-diffluence, Rio Paraná, Argentina, *Earth Surf. Processes Landforms*, *32*(1), 155–162, doi:10.1002/esp.1457.

Parsons, D. R., P. R. Jackson, J. A. Czuba, F. L. Engel, B. L. Rhoads, K. A. Oberg, J. L. Best, D. S. Mueller, K. K. Johnson, and J. D. Riley (2013), Velocity mapping toolbox (VMT): A processing and visualization suite for moving-vessel aDcp measurements, *Earth Surf. Processes Landforms*, *38*(11), 1244–1260, doi:10.1002/esp.3367.

Reid, I., J. T. Layman, and L. E. Frostick (1980), The continuous measurement of bed load discharge, *J. Hydraul. Res.*, *18*, 243–249.

Rennie, C. D. (2012), Mapping water and sediment flux distributions in gravel bed rivers using aDcps, in *Gravel Bed Rivers: Processes, Tools, Environments*, edited by M. Church, P. M. Biron, and A. G. Roy, John Wiley, Chichester, U. K., doi:10.1002/9781119952497.ch25.

Rennie, C. D., and M. Church (2010), Mapping spatial distributions and uncertainty of water and sediment flux in a large gravel bed river reach using an acoustic Doppler current profiler, *J. Geophys. Res.*, *115*, F03035, doi:10.1029/2009JF001556.

Rennie, C. D., and R. G. Millar (2004), Measurement of the spatial distribution of fluvial bed load transport velocity in both sand and gravel, *Earth Surf. Processes Landforms*, *29*(10), 1173–1193, doi:10.1002/esp.1074.

Rennie, C. D., and R. Millar (2007), Deconvolution technique to separate signal from noise in gravel bed load velocity data, *J. Hydraul. Eng.*, *133*(8), 845–856, doi:10.1061/(ASCE)0733-9429(2007)133:8(845.

Rennie, C. D., and F. Rainville (2006), Case study of precision of GPS differential correction strategies: Influence on aDcp velocity and discharge estimates, *J. Hydraul. Eng.*, *132*(3), 225–234, doi:10.1061/(asce)0733-9429(2006)132:3(225).

Rennie, C. D., and P. V. Villard (2004), Site specificity of bed load measurement using an acoustic Doppler current profiler, *J. Geophys. Res.*, *109*, F03003, doi:10.1029/2003JF000106.

Rennie, C. D., R. Millar, and M. Church (2002), Measurement of bed load velocity using an acoustic Doppler current profiler, *J. Hydraul. Eng.*, *128*(5), 473–483, doi:10.1061/(asce)0733-9429(2002)128:5(473).

Rickenmann, D., J. M. Turowski, B. Fritschi, A. Klaiber, and A. Ludwig (2012), Bed load transport measurements at the Erlenbach stream with geophones and automated basket samplers, *Earth Surf. Processes Landforms*, *37*(9), 1000–1011, doi:10.1002/esp.3225.

Riley, J. D., and B. L. Rhoads (2012), Flow structure and channel morphology at a natural confluent meander bend, *Geomorphology*, *163–164*, 84–98, doi:10.1016/j.geomorph.2011.06.011.

Schuurman, F., W. A. Marra, and M. G. Kleinhans (2013), Physics-based modeling of large braided sand bed rivers: Bar pattern formation, dynamics, and sensitivity, *J. Geophys. Res. Earth Surf.*, *118*, 2509–2527, doi:10.1002/2013JF002896.

Szupiany, R. N., M. L. Amsler, D. R. Parsons, and J. L. Best (2009), Morphology, flow structure, and suspended bed sediment transport at two large braid-bar confluences, *Water Resour. Res.*, *45*, W05415, doi:10.1029/2008WR007428.

Szupiany, R. N., M. L. Amsler, J. Hernandez, D. R. Parsons, J. L. Best, E. Fornari, and A. Trento (2012), Flow fields, bed shear stresses, and suspended bed sediment dynamics in bifurcations of a large river, *Water Resour. Res.*, *48*, W11515, doi:10.1029/2011WR011677.

Teledyne RD Instruments (2010), aDcp coordinate transformation: Formulas and transformations.

Thompson, S. M. (1985), Transport of gravel by flows up to 500 m^3/s, Ohau River, Otago, New Zealand, *J. Hydraul. Res.*, *23*(3), 285–303, doi:10.1080/00221688509499356.

Tsubaki, R., Y. Kawahara, Y. Muto, and I. Fujita (2012), New 3-D flow interpolation method on moving aDcp data, *Water Resour. Res.*, *48*, W05539, doi:10.1029/2011WR010867.

Vericat, D., and R. J. Batalla (2010), Sediment transport from continuous monitoring in a perennial Mediterranean stream, *CATENA*, *82*(2), 77–86, doi:10.1016/j.catena.2010.05.003.

Vericat, D., M. Church, and R. J. Batalla (2006), Bed load bias: Comparison of measurements obtained using two (76 and 152 mm) Helley-Smith samplers in a gravel bed river, *Water Resour. Res.*, *42*, W01402, doi:10.1029/2005WR004025.

Villard, P., Church, M., and Kostaschuk, R. (2005), Estimating bed load in sand bed channels using bottom tracking from an acoustic Doppler profiler, in *Fluvial Sedimentology VII*, edited by M. D. Blum, S. B. Marriott, and S. F. Leclair, Blackwell Ltd., Oxford, U. K., doi:10.1002/9781444304350.ch12.

Warburton, J. (1992), Observations of bed load transport and channel bed changes in a proglacial mountain stream, *Arct. Alp. Res.*, *24*(3), 195–203, doi:10.2307/1551657.

Wheaton, J. M., J. Brasington, S. E. Darby, and D. A. Sear (2010), Accounting for uncertainty in DEMs from repeat topographic surveys: Improved sediment budgets, *Earth Surf. Processes Landforms*, *35*(2), 136–156, doi:10.1002/esp.1886.

Wheaton, J. M., J. Brasington, S. E. Darby, A. Kasprak, D. Sear, and D. Vericat (2013), Morphodynamic signatures of braiding mechanisms as expressed through change in sediment storage in a gravel bed river, *J. Geophys. Res. Earth Surf.*, *118*, 759–779, doi:10.1002/jgrf.20060.

Wilcock, P. R., S. T. Kenworthy, and J. C. Crowe (2001), Experimental study of the transport of mixed sand and gravel, *Water Resour. Res.*, *37*(12), 3349–3358, doi:10.1029/2001WR000683.

Williams, R. D. (2012), DEMs of Difference, in *Geomorphological Techniques (Online Edition)*, edited by L. E. Clarke, British Society for Geomorphology. [Available at http://www.geomorphology.org.uk/assets/publications/subsections/pdfs/OnsitePublicationSubsection/14/2.3.2_demsofdifference.pdf.]

Williams, R. D., J. Brasington, D. Vericat, D. M. Hicks, F. Labrosse, and M. Neal (2011), Monitoring braided river change using terrestrial laser scanning and optical bathymetric mapping, in *Geomorphological Mapping: Methods and Applications*, edited by M. Smith, P. Paron, and J. Griffiths, pp. 507–532, Elsevier, Amsterdam, doi:10.1016/B978-0-444-53446-0.00020-3.

Williams, R. D., J. Brasington, M. Hicks, R. Measures, C. D. Rennie, and D. Vericat (2013), Hydraulic validation of two-dimensional simulations of braided river flow with spatially continuous aDcp data, *Water Resour. Res.*, *49*, 5183–5205, doi:10.1002/wrcr.20391.

Williams, R. D., J. Brasington, D. Vericat, and D. M. Hicks (2014), Hyperscale terrain modeling of braided rivers: Fusing mobile terrestrial laser scanning and optical bathymetric mapping, *Earth Surf. Processes Landforms*, *39*(2), 167–183, doi:10.1002/esp.3437.

Wolman, M. G. (1954), A method of sampling coarse bed material, *Trans., Am. Geophys. Union*, *35*, 951–956.

Ziliani, L., N. Surian, T. J. Coulthard, and S. Tarantola (2013), Reduced-complexity modeling of braided rivers: Assessing model performance by sensitivity analysis, calibration, and validation, *J. Geophys. Res. Earth Surf.*, *118*, 2243–2262, doi:10.1002/jgrf.20154.